Time-Resolved Spatial Measurements of Gravity-Capillary Waves

T. Bhirawa[1], Kevin[1], J. H. Lee[1] and J. P. Monty[1]

[1]Department of Mechanical Engineering the University of Melbourne, Parkville, Victoria 3010, Australia

Abstract

An experimental study measuring temporally resolved two-dimensional surface elevation of wind-generated gravity-capillary waves is discussed. We employed a laser illumination and image-based technique to investigate the wave surface evolution and the associated interaction between waves which have different wavelength and phase speed. The surface elevations are obtained from the images using a dynamic threshold algorithm, which is based on bi-modality analysis of the intensity histogram. This method is less complicated compared with the stereo-imaging technique for the reconstruction of the wave surface. Results show that the linear dispersion relationship under-predicts the wave peak celerity while the frequency-converted wavenumber spectra shows an apparent differences compared with the 'true' wavenumber spectra from spatial measurements. An analysis of instantaneous phase velocities associated with waves with a range of wavelengths reveals small-scale waves have two distinct phase velocities. The small wavelength waves either follow the phase velocity of the dominant waves at higher wind speed or the gravity-capillary dispersion theory at lower wind speed.

Introduction

A better understanding of the interaction between large and small-scale wind-waves across the spectrum is essential for ocean modelling. Commonly, wind-waves are represented by statistics and spectral parameters. This generally assumes that ocean waves are a summation of harmonic waves with different scales which have certain characteristics and interaction between the large and small-scale waves. In the literature, it has been suggested that the presence of large-scale waves affects the growth of wind-waves and air-sea momentum transfer [7, 9, 13], while has little effect on roughness length [13, 14]. On the other hand, the small-scale waves act as the surface roughness element of ocean waves, more specifically the gravity-capillary waves [4, 10, 14]. Laxague *et al.* (2015) argued that the gravity-capillary waves are the greatest contributor of sea surface roughness. Moreover, while their role in the wind-wave growth and wave breaking is important, the relationship with longer wave is less certain. Waves in deep water are often studied using the linear wave theory (Airy wave theory), which requires the dispersion relationship:

$$\omega^2 = gk \ \tanh(kd) \tag{1}$$

where $\omega = 2\pi f$, is the wave angular frequency, $k = 2\pi/L$ is the wavenumber, g is the gravity acceleration and d is the water depth. However, due to the strong influence of surface tension, the small-scale gravity-capillary waves follow the modified dispersion relationship [15]:

$$\omega^2 = k \ (g + \sigma k^2/\rho) \tag{2}$$

where ρ is the water density and σ is the surface tension. Several studies have also revealed the modulation of small-scale by large-scale waves [2, 9, 11, 13]. The modulation effect could either enhance [5, 6] or suppress the small-scale waves [12, 13].

The interaction between wave of different scales could also be seen when measuring the wind-waves using both spatial and temporal analysis. The frequency spectrum from temporal analysis failed to capture intrinsic spectrum of small-scale waves [16]. This could be clearly seen when the measured wavenumbers are compared with the linear theory values [3, 15].

In this study we document new spatio-temporal measurements using a laser-sheet illumination method similar to Perlin et al. (1993) in both the stream-wise and span-wise direction. The objective of the study is to capture the fine details of waves at different wind speeds as well as cover sufficiently large range of wave scales. Furthermore, the analysis of both spatial and temporal spectra will be compared as well as the relationship with the well-established linear wave theory. The interaction between waves of different scales will also be reported.

Experimental Setup

Method and Facility

Non-intrusive two-dimensional spatio-temporal experiments were carried out by Perlin *et al.* (1993) to investigate the generation of small-scale capillary waves by large-scale gravity waves. The 3D reconstruction of the wind-wave field was attempted by Zavadsky *et al.* (2017) in a closed-controlled laboratory experiment using the stereo-imaging technique. The application of the stereographic technique is difficult in terms of illumination and space requirement. While the stereo-imaging method was able to produce 3D instantaneous reconstructions of wind-wave field, it is less sensitive to the small-scale waves [1, 15].

The surface wave measurements were carried out using the laser-illumination technique in the wave flume at the Sea Ice Wind Wave Interaction (SIWWI) facility, the University of Melbourne. The wave flume has a wind-tunnel built over its length. It is 14 m long, 0.75 wide and 0.7 m high and filled with water up to a depth of 0.3 m, as shown in Figure 1. It consists of 1:3 ratio of contraction and a series of flow conditioners at the inlet. The acrylic roof panels are angled to reduce the pressure gradient. An exit diffuser is placed at the outlet with a suction fan to generate the wind-waves. The wind-waves are generated at a range of wind speeds from 4 to 8.5 m/s. At the end of the flume, a permeable sloped beach is installed to dissipate incoming waves. The measurement station is 3.5 m from the end of the contraction where the side glass walls enabled optical access to the test section.

Silver-coated hollow glass sphere particles were added to the water and illuminated by sheets of 1 mm thickness continuous laser of 50mW with 532 nm wavelength. The wave surface was recorded using PCO Dimax HS4 cameras which have a resolution of 2000 × 2000 pixels in both the stream-wise and span-wise direction. Throughout this paper, x-, y- and z- denote the stream-wise, span-wise and wall-normal directions of the flow. The camera resolution for x-direction is 86.4 μm per pixel with a sampling rate of 200 Hz, while y-direction has resolution of 75.5 μm per pixel with a sampling rate of 100 Hz. The cameras are angled by 13° for the y-direction (Fig. 2a) to minimize the meniscus effect, and by 30° parallel to the glass is for the x-
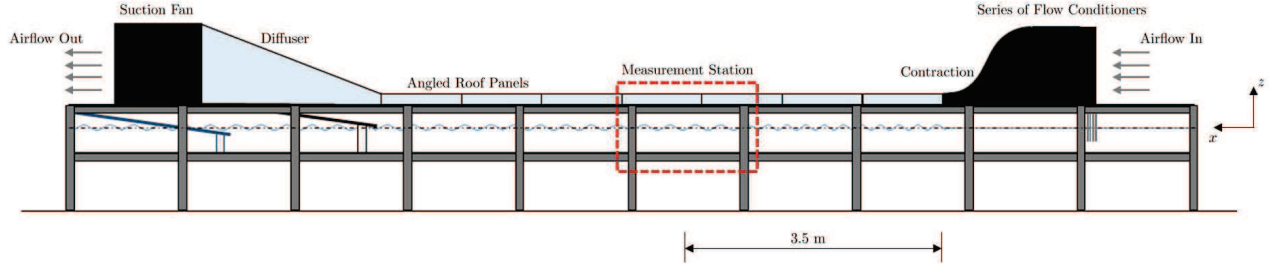
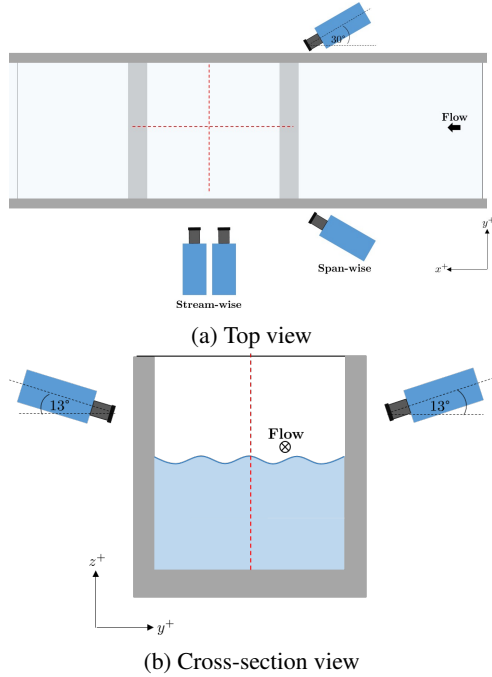Figure 1: Schematic view of wave flume and experimental setup.

(a) Top view

(b) Cross-section view

Figure 2: The surface measurement setup.

Figure 3: Spatio-temporal plot of wave surface $\eta(x,t)$ in the x-direction for $U_\infty = 8.5\,\text{m/s}$.

direction (Fig. 2b). The field of view (FOV) is about 0.35×0.3 m. The waves were measured for 50 and 100 seconds for the x- and y- direction respectively, hence resulted in approximately 10,000 surface realizations for each direction. Table 1 summarises the experimental parameters including the significant wave height (H_s) of each wind speed. The peak wavelengths (λ_p) and peak frequencies (f_p) are determined from the spatial and temporal spectra respectively.

$U_\infty\,(\text{m/s})$	$\lambda_p\,(\text{mm})$	$f_p\,(\text{Hz})$	$H_s\,(\text{mm})$	$C_p\,(\text{mm/s})$
4.0	65	6.37	2.51	370
4.5	80	5.80	4.24	420
5.5	108	4.96	6.61	470
8.5	164	3.98	16.45	580

Table 1: Experimental cases.

Surface Detection

The dynamic-threshold method of surface detection is applied following the Chow and Kaneko (1972). This method relies on the profile of histogram intensity and assumes that the air-water boundary is the region where the histogram is classified as bi-modal. Each peak in the histogram represents the dark and bright regions. The surface wave detection follows sev-
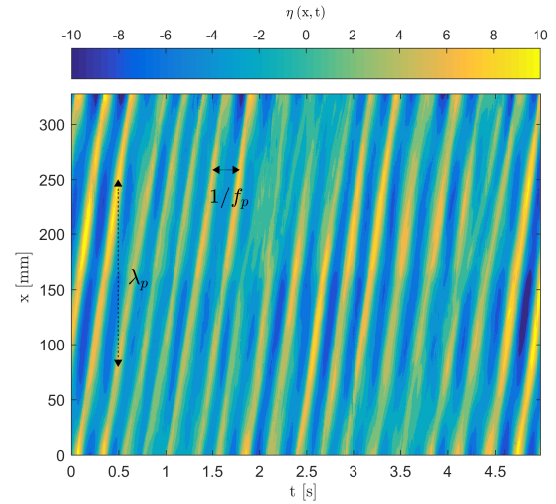
eral steps: firstly, each of the recorded image is separated into smaller domains with a window size of 8 by 16 pixels. From each of the domain, the variance of histogram intensity is calculated. The domains with significantly large variance are further considered for the surface detection. The histogram from the selected domains are then analysed and tested for bi-modality, the profile that has largest difference between peaks within a certain column is determined as the illuminated surface of the waves. Later, the surface is iteratively obtained within the selected domain using locally computed threshold, which is the mean of the local histogram intensity. The accuracy of the detection is about ± 0.7 mm and ± 0.6 mm for the x- and y-direction measurements respectively.

Results and Discussions

In this section, the results from the x-direction will be discussed. An example of the instantaneous surface wave profile in spatial domain $\eta(x)$ at a given time instance is shown in figure 3, as well as the illustration of the peak wavelength (λ_p) and peak frequencie (f_p). The surface map displays diagonal feature which indicates the crests and troughs of waves over time and space. Plotting in this manner reflects how the waves travel in time, along the captured x-direction. The wave celerities are obtained from the slope between the spatial and temporal axis, $C_p = dx/dt$. To illustrate the limitation of dispersion relationship, we convert the energy spectra in the frequency domain to the wavenumber domain following $k = 2\pi f/C_p$, and compare the resulting spectral distribution to the measured wavenumber spectra.
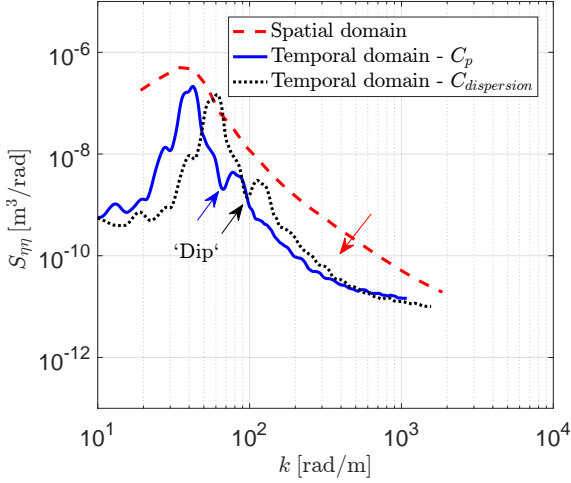
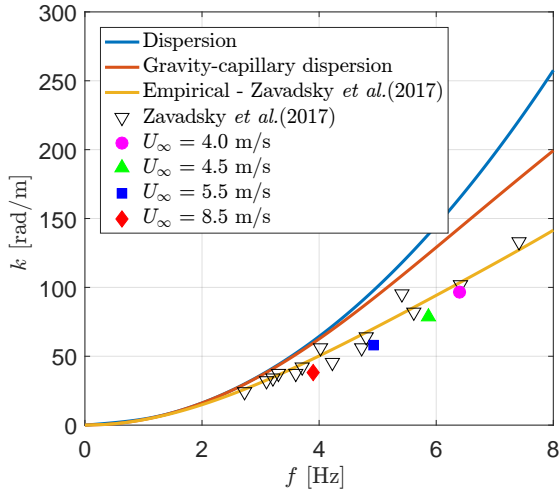Figure 4: Comparison between wavenumber spectra obtained from spatial and temporal analysis for $U_\infty = 8.5$ m/s.

Figure 6: Decomposed frequency spectra for $U_\infty = 8.5$ m/s.

Figure 5: Variation of wavenumber with frequency.
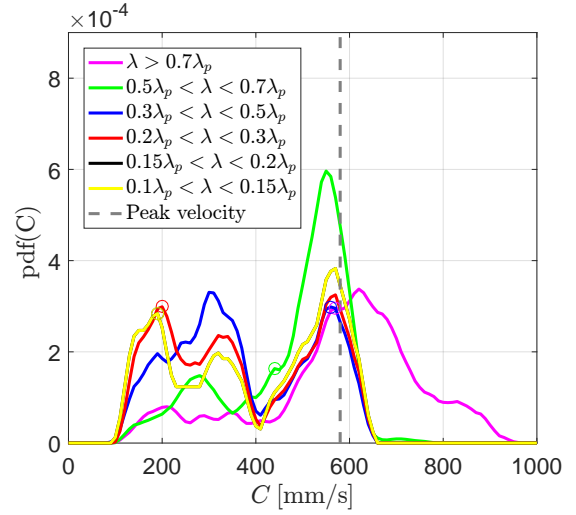
Figure 7: Decomposed phase velocity for $U_\infty = 8.5$ m/s; second peak of velocity (○).

As shown in Figure 4, the spectral comparison is displayed for the highest wind speed of $U_\infty = 8.5$ m/s. It is evident that the frequency-to-wavenumber spectrum (solid-blue line) is intrinsically different from the 'true' wavenumber spectrum (red-dashed line), specifically, there is a unique 'dip' as annotated in Figure 4. The frequency-to-wavenumber conversion using wave celerity from the dispersion relationship in deep water, $C_{disp} = 1.56 f_p$, is shown to overpredict the peak wavenumber (black-dotted line). Furthermore, it seems that the converted spectra underpredict the wavenumber range, as shown by the red-arrow annotation in figure 4. We further compare the corresponding frequencies and wavenumbers of these spectral peaks, and the change in their relationship is displayed in figure 5. Note that the progression of dominant (peak) wavenumber and frequency has been predicted by the dispersion and capillary-gravity dispersion theories [15], where these known relationships are overlaid in figure 5 for comparison. It is clear that the relationship suggested by the present wind-waves deviates from these prediction, particularly for higher frequency data. Here, we also include the data points from Zavadsky *et al.* (2017), where their wind-wave range was comparable to the present ex-
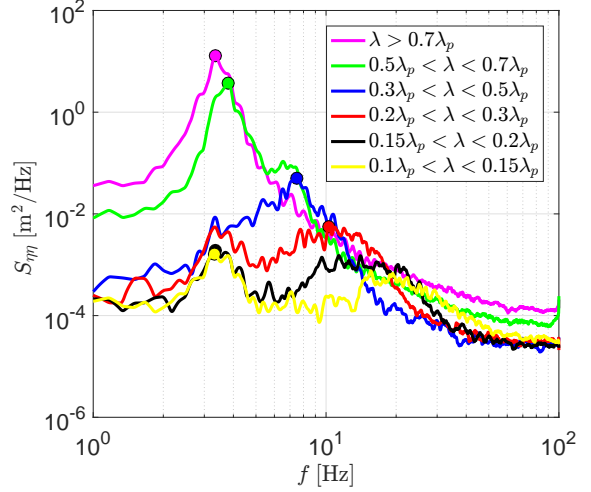
periments. Good agreement is observed for both experimental results, showing a more moderate change in k_p with its frequency. Zavadsky *et al.* (2017) argued that the deviation from the dispersion theory may be influenced by the Doppler shift.

In order to examine further the frequency to wavenumber relationship, the spatio-temporal data is band-pass filtered spatially, prior to computing the frequency spectrum. Figure 6 shows the resulting spectra for several indicated bandwidths. For the long-wavelength signals, a narrow band energy distribution is apparent. For the short-wavelength components however, the frequency spectra are more broadband and bi-modal at smallest-scales. At present, the implication of these different distribution is still inconclusive, though it may be related to the 'dip' in the frequency spectra observed in Figure 4. From the bandwidth-filtered data, we can reproduce the spatio-temporal map similar to figure 3 for every wavelength group. Accordingly, the phase velocity of each group can be characterised using the diagonal features, similar to that described earlier. Figure 7 shows the distribution of the phase velocity for each group of wavelengths. It seems that larger wavelengths convect near the velocity of the dominant waveform, but smaller waves convect at a bi-modal velocity distribution. Note that this behaviour is only
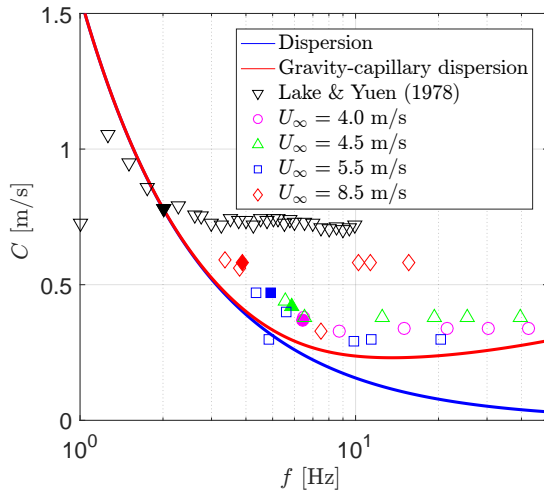
Figure 8: Relationship of phase velocities with frequency: solid color refers to the peak phase velocity.

observed for the highest wind speed case. And for the convection velocities of the remaining cases, the wavelength groups seem to be influenced, if not follow, the dominant-phase velocity. This may reflects the behaviour that shorter waves rides on the longer waves [16], and at higher wind speed, the larger wave is faster leaving the smaller wave behind. The difference in velocity between group of wavelengths is shown in Figure 8. The peak velocity of each group is plotted versus the frequency, while the solid markers indicates the peak velocity of each wind speed case. The results show a good agreement with the gravity-capillary dispersion theory for higher frequency waves. However, for high wind speed case, the small-scale waves are strongly influenced by the dominant wave celerity. Results from Lake & Yuen (1978) also display this similar trend.

Conclusions

A laser illumination technique was performed to obtain the resolved spatio-temporal wave height data-sets with reasonable accuracy. The established dispersion relationship cannot relate the frequency and wavenumber distribution of wind-waves. Furthermore, the wavenumber and frequency spectra have different characteristic shape, particularly the dip in the frequency spectrum, which may be related to the bi-modal distribution for shorter wavelength or the Doppler shift effect. The peak velocity of small-scale wave groups follow the gravity-capillary dispersion relationship, then seem to be influenced by the dominant wave velocity at higher wind speed.

References

[1] Benetazzo, A., Serafino, F., Bergamasco, F., Ludeno, G., Ardhuin, F., Sutherland, P., Sclavo, M. and Barbariol, F., Stereo imaging and x-band radar wave data fusion: An assessment, *Ocean Engineering*, **152**, 2018, 346–352.

[2] Cox, C. S., Measurements of slopes of high-frequency wind waves, *J. Mar. Res.*, **16**, 1958, 199–225.

[3] Donelan, M. A., Drennan, W. and Magnusson, A. K., Nonstationary analysis of the directional properties of propagating waves, *Journal of Physical Oceanography*, **26**, 1996, 1901–1914.

[4] Hara, T., Bock, E. J. and Lyzenga, D., In situ measurements of capillary-gravity wave spectra using a scanning laser slope gauge and microwave radars, *Journal of Geophysical Research: Oceans*, **99**, 1994, 12593–12602.

[5] Hwang, P. A., Microstructure of ocean surface roughness: A study of spatial measurement and laboratory investigation of modulation analysis, *Journal of Atmospheric and Oceanic Technology*, **16**, 1999, 1619–1629.

[6] Hwang, P. A., Phase distribution of small-scale ocean surface roughness, *Journal of physical oceanography*, **32**, 2002, 2977–2987.

[7] Kahma, K. K., Donelan, M. A., Drennan, W. M. and Terray, E. A., Evidence of energy and momentum flux from swell to wind, *Journal of Physical Oceanography*, **46**, 2016, 2143–2156.

[8] Lake, B. M. and Yuen, H. C., A new model for nonlinear wind waves. part 1. physical model and experimental evidence, *Journal of fluid mechanics*, **88**, 1978, 33–62.

[9] Laxague, N. J., Curcic, M., Björkqvist, J.-V. and Haus, B. K., Gravity-capillary wave spectral modulation by gravity waves, *IEEE Transactions on Geoscience and Remote Sensing*, **55**, 2017, 2477–2485.

[10] Laxague, N. J., Haus, B. K., Bogucki, D. and Özgökmen, T., Spectral characterization of fine-scale wind waves using shipboard optical polarimetry, *Journal of Geophysical Research: Oceans*, **120**, 2015, 3140–3156.

[11] Miller, S. J., Shemdin, O. H. and Longuet-Higgins, M. S., Laboratory measurements of modulation of short-wave slopes by long surface waves, *Journal of Fluid Mechanics*, **233**, 1991, 389–404.

[12] Reece, A. M., Modulation of short waves by long waves, *Boundary-Layer Meteorology*, **13**, 1978, 203–214.

[13] Wu, J., Effects of long waves on wind boundary layer and on ripple slope statistics, *Journal of Geophysical Research*, **82**, 1977, 1359–1362.

[14] Wu, J., Roughness elements of the sea surface—their spectral composition, *Tellus A*, **38**, 1986, 178–188.

[15] Zavadsky, A., Benetazzo, A. and Shemer, L., On the two-dimensional structure of short gravity waves in a wind wave tank, *Physics of Fluids*, **29**, 2017, 016601.

[16] Zhang, X., Capillary–gravity and capillary waves generated in a wind wave tank: Observations and theories, *Journal of Fluid Mechanics*, **289**, 1995, 51–82.